ETH zürich

ETH Library

FEM-based elasticity reconstruction using ultrasound for imaging tissue ablation

Journal Article

Author(s):
Otesteanu, Corin F.; Vishnevskiy, Valery; Goksel, Orcun

Publication date:
2018-06

Permanent link:
https://doi.org/10.3929/ethz-b-000261002

Rights / license:
In Copyright - Non-Commercial Use Permitted

Originally published in:
International Journal of Computer Assisted Radiology and Surgery 13(6), https://doi.org/10.1007/s11548-018-1714-x

This page was generated automatically upon download from the ETH Zurich Research Collection.
For more information, please consult the Terms of use.

International Journal of Computer Assisted Radiology and Surgery (2018) 13:885–894
https://doi.org/10.1007/s11548-018-1714-x

ORIGINAL ARTICLE

FEM-based elasticity reconstruction using ultrasound for imaging tissue ablation

Corin F. Otesteanu[1] · Valery Vishnevsky[1] · Orcun Goksel[1]

Received: 30 January 2018 / Accepted: 16 February 2018 / Published online: 17 April 2018
© CARS 2018

Abstract

Purpose Success of ablation treatment depends on the accurate placement of the target ablation focus and the complete destruction of the pathological tissue. Thus, monitoring the formation, location, and size of the ablated lesion is essential. As ablated tissue gets stiffer, an option for ablation monitoring is ultrasound elastography, for imaging the tissue mechanical properties. Reconstruction of elasticity distribution can be achieved by solving an inverse problem from observed displacements, based on a deformable tissue model, commonly discretized by the finite element method (FEM). However, available reconstruction techniques are prone to noise and may achieve suboptimal accuracy.

Methods We propose a novel inverse problem formulation and elasticity reconstruction method, in which both the elasticity parameters and the model displacements are estimated as independent parameters of an unconstrained optimization problem. Total variation regularization of spatial elasticity distribution is introduced in this formulation, providing robustness to noise.

Results Our approach was compared to state of the art direct and iterative harmonic elastography techniques. We employed numerical simulation studies using various noise and inclusion contrasts, given multiple excitation frequencies. Compared to alternatives, our method leads to a decrease in RMSE of up to 50% and an increase in CNR of up to 11 dB in numerical simulations. The methods were also compared on an ex vivo bovine liver sample that was locally subjected to ablation, for which improved lesion delineation was obtained with our proposed method. Our method takes ~ 4 s for 20×20 reconstruction grid.

Conclusions We present a novel FEM problem formulation that improves reconstruction accuracy and inclusion delineation compared to currently available techniques.

Keywords Ultrasound elastography · Optimization · Lesion monitoring

Introduction

Minimally invasive therapy is an attractive alternative to surgery [12,20]. Tissue ablation represents the destruction of pathologic tissue, with the aim to cure a disease [35]. Tissue destruction can be achieved by thermal methods, or by application of chemical substances. Ablation can be used in clinical applications such as treatment of heart arrhythmia [24], uterine bleeding [6] or tumor ablation [10,22].

The clinical application of minimally invasive treatment modalities such as radiofrequency ablation [13,28], microwave ablation [36], cryoablation [19] or high-intensity focused ultrasound [14] is challenging due to lack of intraoperative information such as pathological tissue location and to high dependency on probe or catheter placement [34]. Because the success of ablation treatment depends on the destruction of the pathological tissue, imaging techniques that allow fast pre and post treatment localization of pathological tissues are essential. Monitoring lesions during their formation is essential because the pathological tissue can be targeted accurately and nearby tissues spared. Moreover, real-time monitoring could provide feedback regarding intensity and duration, ensuring that coagulation occurs [32]. Ultrasound is a medical diagnostic modality which allows for

✉ Corin F. Otesteanu
corino@vision.ee.ethz.ch

Valery Vishnevsky
valeryv@vision.ee.ethz.ch

Orcun Goksel
ogoksel@vision.ee.ethz.ch

[1] Computer-Assisted Applications in Medicine Group, Swiss Federal Institute of Technology (ETH Zurich), 8092 Zurich, Switzerland

in-vivo, real-time imaging of tissue [18]. Ultrasound elastography is a particularly useful technique, as it measures tissues elasticity and is not affected by increased echogenicity due to ablation, which could impede proper lesion delineation [23]. Techniques such as strain imaging [29], harmonic elastography [33], shear wave elastography [1] and speed of sound imaging [3] can be used to measure tissue elasticity and monitor ablation.

In this paper, we used harmonic elastography and the finite element method (FEM) to monitor tissue elasticity for lesion delineation. There are a variety of FEM-based methods in literature, which can be divided into direct and iterative methods. In the direct methods [15,27], a closed-form solution of the inverse problem of elasticity is calculated directly in a least square sense under certain assumptions. In the iterative methods [7,8], the inverse problem is considered an optimization problem, and the elasticity parameter distribution is changed iteratively to minimize the error between measured and model displacements.

We propose a novel inverse problem formulation in which both the elasticity parameters and the reconstructed displacements are estimated as independent parameters of an unconstrained optimization problem. We evaluated our method on various numerical simulations and compare it to the direct and iterative approaches. Finally, the method was tested on an ex vivo ablated bovine liver sample.

Methods

The equation of motion for an elastic isotropic and linear material is given by [16]:

$$\nabla \cdot [\mu(\nabla u + (\nabla u)^T) + \gamma(\nabla \cdot u)I] = \rho \ddot{u}. \tag{1}$$

Here, μ is the shear modulus, u is the displacement vector, ρ is the density of the material, ω is the excitation frequency, and γ is the first Lame parameter. Equation (1) can be discretized using the finite element method (FEM) [37] and, considering harmonic motion, written in Fourier domain as

$$\left[\mathbf{K}(\boldsymbol{\mu}, \boldsymbol{\gamma}) - \omega^2 \mathbf{M}(\boldsymbol{\rho})\right] \cdot \hat{\mathbf{u}} = \hat{\mathbf{f}}, \tag{2}$$

where $\mathbf{K}$ is the stiffness matrix, which is a function of the elasticity parameter vectors $\boldsymbol{\mu}$ (Shear modulus) and $\boldsymbol{\nu}$ (Poisson's ratio); $\mathbf{M}$ is the mass matrix, as a function of density $\boldsymbol{\rho}$; $\boldsymbol{\omega}$ is the angular excitation frequency [37]; and $\hat{\boldsymbol{u}}$ and $\hat{\boldsymbol{f}}$ are the displacement and force phasors, respectively. Since density does not vary much in tissue [31], a known constant value ($\approx$1000 kg/m^3) can be used for $\boldsymbol{\rho}$.

In nearly incompressible materials (i.e., $\nu \to 0.5$), a problem called *locking* may occur in the FEM integration that yields over-stiff elements [2]. To overcome this, a mixed displacement-pressure formulation of the FEM was proposed [17]

$$\begin{bmatrix} \boldsymbol{K_\mu}(\boldsymbol{\mu}) - \omega^2 \mathbf{M} & \boldsymbol{K_p} \end{bmatrix} \cdot \begin{bmatrix} \hat{\mathbf{u}} \\ \hat{\mathbf{p}} \end{bmatrix} = \begin{bmatrix} \hat{\mathbf{f}} \end{bmatrix}, \tag{3}$$

where $\boldsymbol{p}$ is the pressure term and the stiffness matrix $\boldsymbol{K}$ is written as split in two matrices $\boldsymbol{K_\mu}$ and $\boldsymbol{K_p}$, which correspond to the shear modulus and pressure term, respectively. Using an imaging modality, the displacements in the region of interest are observed, where we denote these measured displacements by $\boldsymbol{d}$. Then, a reconstruction method aims to fit the displacements $\boldsymbol{u}$ estimated by a model to these observed displacements $\boldsymbol{d}$, by optimizing the model parameters, i.e. elastic distribution. Below, we provide a brief summary of existing reconstruction methods, prior to introducing our proposed method.

Direct methods

In the direct methods, the measured displacement are re-substituted as the model estimates, i.e. $\hat{\boldsymbol{u}} = \hat{\boldsymbol{d}}$, which neglects the noise on displacement observations. The system of equations (3) is then rearranged with respect to the unknown shear modulus and pressure terms, resulting in a linear equation that can be solved in a closed form:

$$\begin{bmatrix} \boldsymbol{K_u}(\hat{\boldsymbol{d}}) & \boldsymbol{K_p} \end{bmatrix} \cdot \begin{bmatrix} \hat{\boldsymbol{\mu}} \\ \hat{\boldsymbol{p}} \end{bmatrix} = \begin{bmatrix} \hat{\mathbf{f}} + \omega^2 \mathbf{M} \hat{\boldsymbol{d}} \end{bmatrix}. \tag{4}$$

Here, $\boldsymbol{K_u}(\boldsymbol{u})$ is the result of reshuffling (3). To improve robustness of the inversion, it is essential to add regularization to (4). Different regularization techniques have been used, such as Tikhonov regularization [27] and sparsity regularization [17]. Here, we used a Tikhonov regularization, by augmenting (4) in the following way:

$$\begin{bmatrix} \boldsymbol{K_u}(\boldsymbol{u}) & \boldsymbol{K_p} \\ \lambda \boldsymbol{\Delta} & 0 \end{bmatrix} \cdot \begin{bmatrix} \hat{\boldsymbol{\mu}} \\ \hat{\boldsymbol{p}} \end{bmatrix} = \begin{bmatrix} \hat{\mathbf{f}} + \omega^2 \mathbf{M} \\ 0 \end{bmatrix}. \tag{5}$$

where $\boldsymbol{\Delta}$ is the discrete Laplace operator and λ is the regularization parameter. Equation (5) is then solved for elastic parameters in the least squares sense.

Iterative methods

In iterative methods, the model displacements are considered to be unknown and the goal of the inverse problem (IP) is to find the elastic parameters that approximate measured displacements, i.e. $\hat{\boldsymbol{u}} \approx \hat{\boldsymbol{d}}$. The IP can be formulated as an optimization problem [8,11], to find the optimal $\boldsymbol{\mu}^\star$ that minimizes the residual between the measured displacements $\hat{\boldsymbol{d}}$ and the model displacements $\hat{\boldsymbol{u}}(\boldsymbol{\mu})$, defined by Eq. (2):

$$\boldsymbol{\mu}^{\star} = \underset{\mu \geq 0}{\operatorname{argmin}} ||\hat{\boldsymbol{u}}(\boldsymbol{\mu}) - \hat{\boldsymbol{d}}||_2^2 + \lambda ||\boldsymbol{\Delta\mu}||_2^2. \tag{6}$$

At each iteration of this optimization problem, the model displacement $\hat{\boldsymbol{u}}$ was updated by inverting (2), using current estimate of the elastic parameters. In this study, we used the reflective trust region [5] to solve the problem in (6).

Proposed hybrid method

Herein, we propose a hybrid method. Similarly to the iterative method, the model displacements are considered unknown; however, they are not parametrized as a function of elastic parameters, but both elastic parameters and model displacements are solved as separate variables. For this, we formulate the following optimization problem:

$$\begin{aligned} &\underset{\boldsymbol{\mu}\geq 0, \hat{\boldsymbol{u}}, \boldsymbol{p}}{\operatorname{argmin}} \frac{1}{2\rho} ||\hat{\boldsymbol{u}} - \hat{\boldsymbol{d}}||_2^2 + ||(\boldsymbol{K}_{\boldsymbol{\mu}}(\boldsymbol{\mu}) - \omega^2 \mathbf{M})\hat{\boldsymbol{u}} \\ &\quad + \boldsymbol{K}_{\boldsymbol{p}}\boldsymbol{p}||_2^2 + \lambda ||\boldsymbol{D\mu}||_1 \\ &\quad = \arg\min F_{\text{cost}}(\boldsymbol{\mu}, \hat{\boldsymbol{u}}, \boldsymbol{p}), \end{aligned} \tag{7}$$

where the first part is the data fidelity term weighted by $\frac{1}{2\rho}$, the second part is the FEM discretized motion equation, and the third part is the anisotropic total variation term, where $\boldsymbol{D}$ is a sparse matrix that implements finite differences in spatial domain, and λ controls the amount of spatial coherence. This optimization problem is nonlinear and non-convex with a non-differentiable cost function due to the ℓ_1 norm used, and hence, the global optimality of a solution cannot be guaranteed. Nevertheless, in practice, gradient-based optimization methods have been used [21]. In this paper, we used the limited-memory BFGS solver provided by `minFunc` package.[1] LBFGS is the quasi-Newton unconstrained optimization method that maintains a low-rank approximation of the Hessian matrix to achieve improved convergence. The gradients of the cost function (7) were calculated as follows:

$$\boldsymbol{G}_{\text{cost}} = \left[\frac{\partial F_{\text{cost}}}{\partial \hat{\boldsymbol{u}}}, \frac{\partial F_{\text{cost}}}{\partial \boldsymbol{\mu}}, \frac{\partial F_{\text{cost}}}{\partial \boldsymbol{p}} \right], \tag{8}$$

$$\begin{aligned} \frac{\partial F_{\text{cost}}}{\partial \hat{\boldsymbol{u}}} &= \frac{1}{\rho}(\hat{\boldsymbol{u}} - \hat{\boldsymbol{d}}) + (\boldsymbol{K}_{\boldsymbol{\mu}}(\boldsymbol{\mu}) - \omega^2 \mathbf{M})^T \\ &\quad (\boldsymbol{K}_{\boldsymbol{\mu}}((\boldsymbol{\mu}) - \omega^2 \mathbf{M})\hat{\boldsymbol{u}} + \boldsymbol{K}_{\boldsymbol{p}}\boldsymbol{p}), \end{aligned} \tag{9}$$

$$\begin{aligned} \frac{\partial F_{\text{cost}}}{\partial \boldsymbol{\mu}} &= \boldsymbol{K}_{\boldsymbol{u}}(\boldsymbol{u})^T (\boldsymbol{K}_{\boldsymbol{u}}(\boldsymbol{u})\boldsymbol{\mu} - \omega^2 \mathbf{M}\hat{\boldsymbol{u}} + \boldsymbol{K}_{\boldsymbol{p}}\boldsymbol{p}) \\ &\quad + \lambda \boldsymbol{D}^T \operatorname{sign}(\boldsymbol{D\mu}), \end{aligned} \tag{10}$$

$$\frac{\partial F_{\text{cost}}}{\partial \boldsymbol{p}} = \boldsymbol{K}_{\boldsymbol{p}}{}^T (\boldsymbol{K}_{\boldsymbol{u}}(\boldsymbol{u})\boldsymbol{\mu} - \omega^2 \mathbf{M}\hat{\boldsymbol{u}} + \boldsymbol{K}_{\boldsymbol{p}}\boldsymbol{p}). \tag{11}$$

[1] M. Schmidt. minFunc: unconstrained differentiable multivariate optimization in Matlab. http://www.cs.ubc.ca/~schmidtm/Software/minFunc.html, 2005.

We also compare the LBFGS solver to the alternating direction method of multipliers (ADMM) [26], which implements a series of proximal mappings to solve (7) based on the following constrained problem formulation:

$$\begin{aligned} \underset{\boldsymbol{\mu}\geq 0, \hat{\boldsymbol{u}}, \boldsymbol{p}, z}{\operatorname{argmin}} \quad & \frac{1}{2\rho} ||\hat{\boldsymbol{u}} - \hat{\boldsymbol{d}}||_2^2 + ||(\boldsymbol{K}_{\boldsymbol{\mu}}(\boldsymbol{\mu}) - \omega^2 \mathbf{M})\hat{\boldsymbol{u}} + \boldsymbol{K}_{\boldsymbol{p}}\boldsymbol{p}||_2^2 \\ & + \lambda ||z||_1, \\ \text{s.t.} \quad & \boldsymbol{D\mu} - z = \mathbf{0}. \end{aligned} \tag{12}$$

Experiments and results

Simulation framework and evaluation metrics

To test our method, we used 40 mm × 40 mm 2-D phantoms, that approximate the field of view of a linear-array ultrasound transducer. The density and Poisson's ratio of the phantoms was chosen to be similar to tissue values: 1000 kg/m^3 and 0.499, respectively. Three phantoms shown in Fig. 1 were simulated: (a) a homogeneous phantom with a Young's modulus of 4 kPa, chosen to mimic healthy liver tissue [9], (b) phantom with a 10 mm radius circular inclusion of 8 kPa, which is a representative value for liver fibrosis [4], (c) phantom with three 4 mm radius inclusions of 2, 8 and 12 kPa, to capture common values for various pathologies [30]. For all simulations, the phantoms were displacement constrained at the bottom edges, while being excited harmonically in the axial direction on the top surface. Simulated groundtruth displacement data ($\hat{\boldsymbol{d}}_T$) was obtained from the numerical phantoms, using (2) and the aforementioned boundary conditions. To simulate noise in the acquisition process, different levels of Gaussian noise were added to the groundtruth displacements, yielding simulated observed displacements $\hat{\boldsymbol{d}}$.

A 40 × 40 mesh with 4 node rectangular elements was used for all reconstructions. The reconstruction quality was quantitatively evaluated using the root-mean-squared error (RMSE) between estimated elasticities $\boldsymbol{\mu}$ and the known groundtruth $\boldsymbol{\mu}_T$. Contrast-to-noise ratio (CNR) was used to measure sharpness of the reconstruction.

$$\text{RMSE} = \frac{\|\boldsymbol{\mu} - \boldsymbol{\mu}_T\|_2}{\sqrt{n}} \tag{13}$$

$$\text{CNR} = \frac{2(\boldsymbol{\mu}_{\text{inc}} - \boldsymbol{\mu}_{\text{bg}})^2}{\sigma_{\text{inc}}^2 + \sigma_{\text{bg}}^2} \tag{14}$$

where $\boldsymbol{\mu}_{\text{inc}}$ and $\boldsymbol{\mu}_{\text{bg}}$ are mean elasticity values of the inclusion and background regions, respectively, while σ_{inc} and σ_{bg} are their corresponding standard deviations.

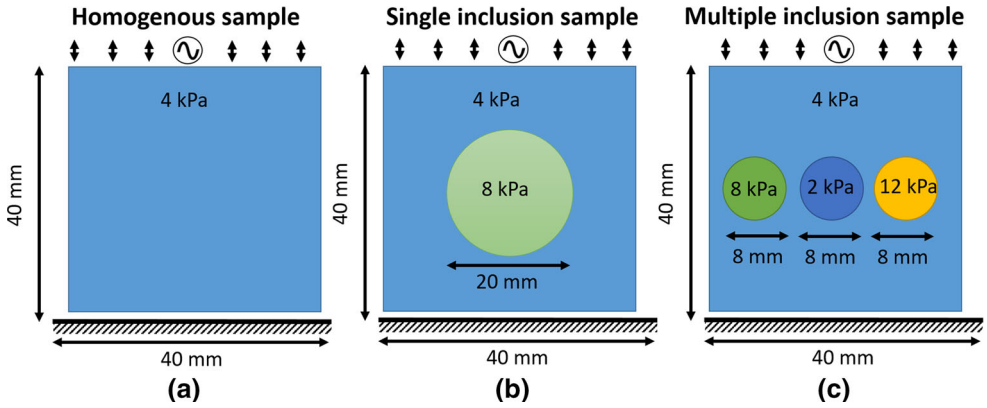

Fig. 1 Numerical models for simulation studies with fixed bottom and harmonically oscillating top boundaries. Three 40 mm × 40 mm numerical phantoms were simulated: **a** homogeneous phantom of 4 kPa, **b** single 10 mm radius inclusion of 8 kPa, and **c** three 4 mm radius inclusions of 8, 2, and 12 kPa

Parameter sensitivity

The convergence of our proposed method was tested using displacement data obtained from the numerical phantom in Fig. 1b by varying the initialization values of elasticity $\boldsymbol{\mu}$ and pressure $\boldsymbol{p}$. Both parameters were initialized by homogeneous maps with values ranging from 2 to 20 kPa in steps on 2 kPa, i.e. $\boldsymbol{\mu} = \boldsymbol{p} = \{2, 4, .., 20\}$. The model displacements were initialized with the simulated displacement, i.e. $\hat{\boldsymbol{u}} = \hat{\boldsymbol{d}}$. Due to nonconvexity of our hybrid formulation (7), LBFGS is not theoretically guaranteed to find the global minimum. However, the results shown in Fig. 2 indicate that our method converges to the same function cost and RMSE from different initializations, given sufficient number of iterations. It can also be seen that initializing with physically plausible values of 4 and 6 kPa yields the fastest convergence rate. We also observe that ADMM solver achieved similar reconstruction quality to LBFGS (see Fig. 3), while ADMM was approximately 6 times slower (21.2 s for ADMM vs. 3.7 s for LBFGS for a reconstruction on a 20 × 20 grid). Therefore, we are using LBFGS to solve (7) in further experiments. To determine the optimal model parameter set, we varied the data fidelity weight ρ on a logarithmic scale between 10^{-3} and 10^{-10}, and the regularization weight (λ) between 10^{-3} and 10^{2}. Reconstructions were run for all aforementioned parameter combinations ($\approx$ 1024 simulations) on the numerical phantom in Fig. 1b. The variation of the residual of the data fidelity term of the optimization cost function are reported for varying parameter settings in Fig. 4a.

To test whether the model coefficients that minimize the residual of the data fidelity term are also the ones leading to correct reconstructions, we computed RMSE of all these reconstructions, given different acquisition noise levels. For each dataset, the method was applied as in the aforementioned case, by varying the model parameters ρ and λ. The RMSE values of the reconstruction can be seen in Fig. 4b. We observe that for high SNR level ($>$ 30 dB) there is a large set of parameter combinations that lead to accurate reconstructions ($<$ 0.2 RMSE). An increase in the noise level leads to an increase in RMSE values, and the optimal parameter region becomes narrower. Results from Fig. 4a, b show that parameter values that provide high data fidelity also result in higher reconstruction accuracy. This observation gives a practical approach to parameter tuning. In Fig. 4c the RMSE for ideal parameter values (in terms of minimum RMSE) for each noise level was compared to those with the parameter values determined unsupervised based on the minimum residual from Fig. 4a.

Numerical phantom results

In our simulation study, we first compared the RMSE of the Direct, Iterative, and the proposed Hybrid methods on the homogeneous 4 kPa phantom in Fig. 1a in a noise-free environment, see Fig. 5a. Gaussian noise was added to the displacement data for an SNR of 30 dB in axial direction and 10 dB in lateral direction, to simulate noise levels similar to ultrasound acquisition with results seen in Fig. 5b. To test the robustness of the methods in noisier conditions, that can occur during clinical settings such as RF ablation, we conducted another experiment at an even higher noise level of 10 dB SNR in both axes; see results in Fig. 5c. Note that as the pixel size was kept constant, an increase in frequency corresponds to an increase in the r ratio. For these noise experiments, 10 random realizations were generated with the mean values and standard deviations depicted in the result in Fig. 5.

As noted in [16], the frequency of excitation, as well as the wavelength of the harmonic wave induced in the tissue is an important parameter for reconstruction. The wavelength is related to the excitation frequency and elasticity, i.e. $\Lambda \propto$

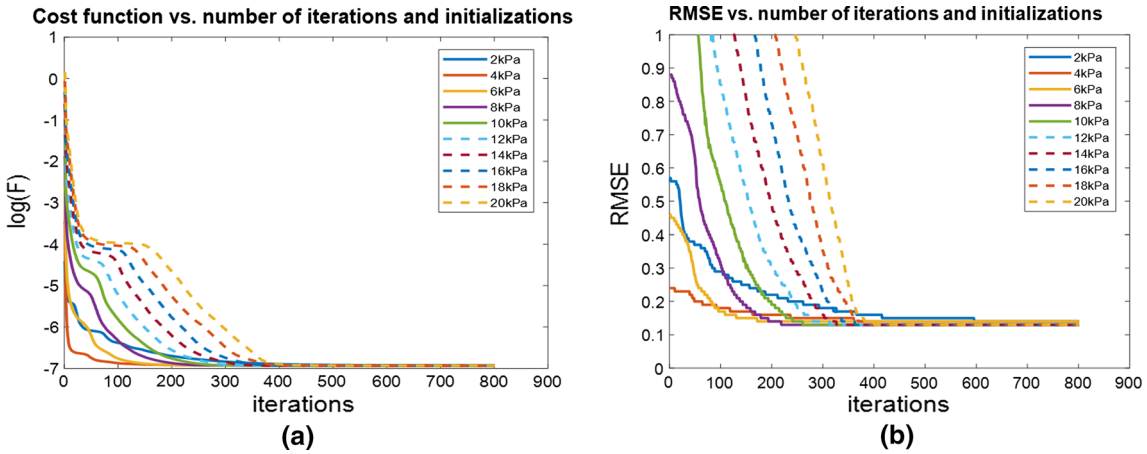

Fig. 2 The optimization cost function value (**a**) and RMSE of current estimate to the ground truth (**b**) at every LBFGS iteration, for different initializations of pressure and elasticity parameters ranging from 2 to 20 kPa

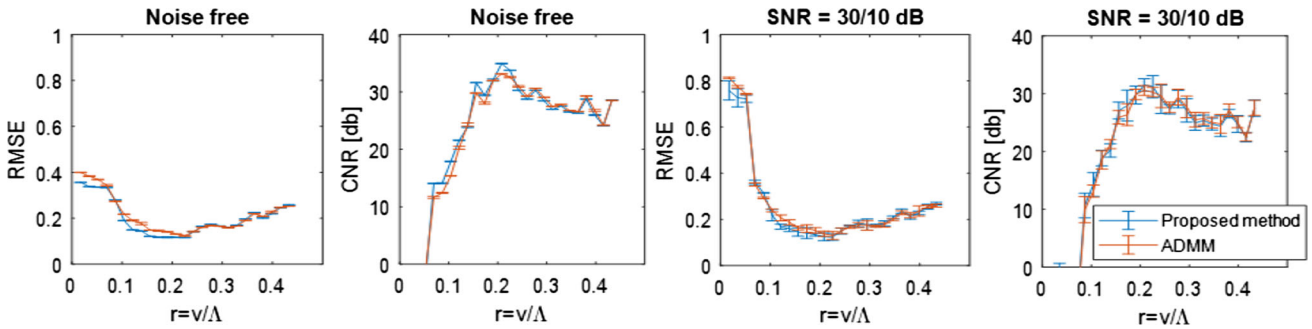

Fig. 3 RMSE and CNR of the reconstructions using the proposed Hybrid method and the ADMM method in the case of a single 8 kPa inclusion inside a 4 kPa phantom for the following cases: noise-free, SNR = 30 dB axial/SNR = 10 dB lateral

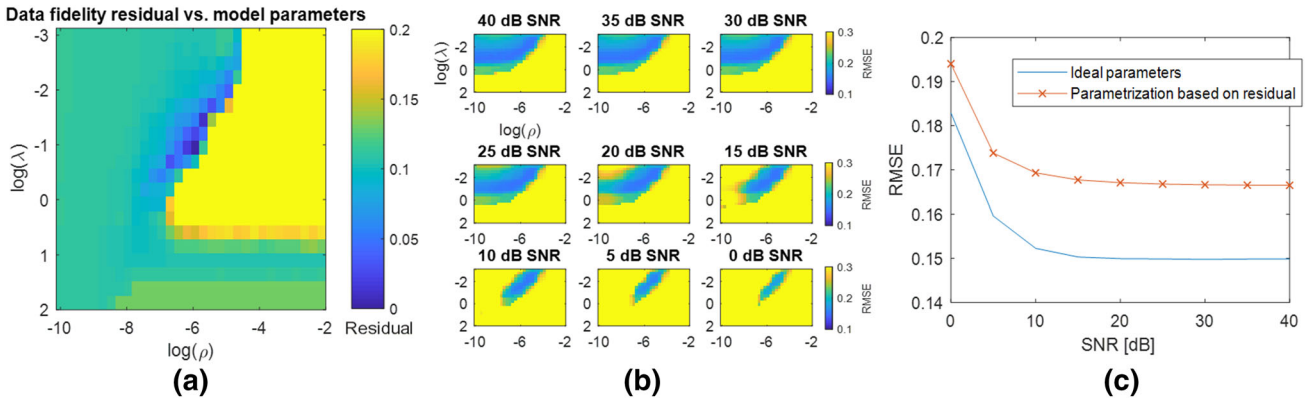

Fig. 4 **a** The residual data fidelity cost $\|\hat{\boldsymbol{u}}^{\star}(\lambda, \rho) - \hat{\boldsymbol{d}}\|_2^2$ plotted against varying model parameters λ and ρ, where an optimal area leading to the minimum residual can be seen in dark blue. **b** RMSE for noise levels ranging between 0 and 40 dB and different values of λ and ρ. **c** Comparison of the RMSE for optimal parameter values and pre-determined values for different noise levels

$\sqrt{\frac{\mu}{\rho}}/f$. Moreover, to be able to compare results with different mesh sizes, the ratio of the voxel size v to wavelength Λ was used during reporting the results, with $r = v/\Lambda$. In all studies, the mesh grid size of 40×40. Excitation frequency was varied between 10 and 500 Hz, in increments of 10 Hz with the upper frequency limit corresponding to ≈ 2.3 mesh grids (pixels) per wavelength.

All three methods gave comparable results for the noise-free case, with ratios $r < 0.25$. Given any noise, the error of the Direct and Iterative methods increase. For the noisy cases, the RMSE decreases rapidly with increasing frequency, until

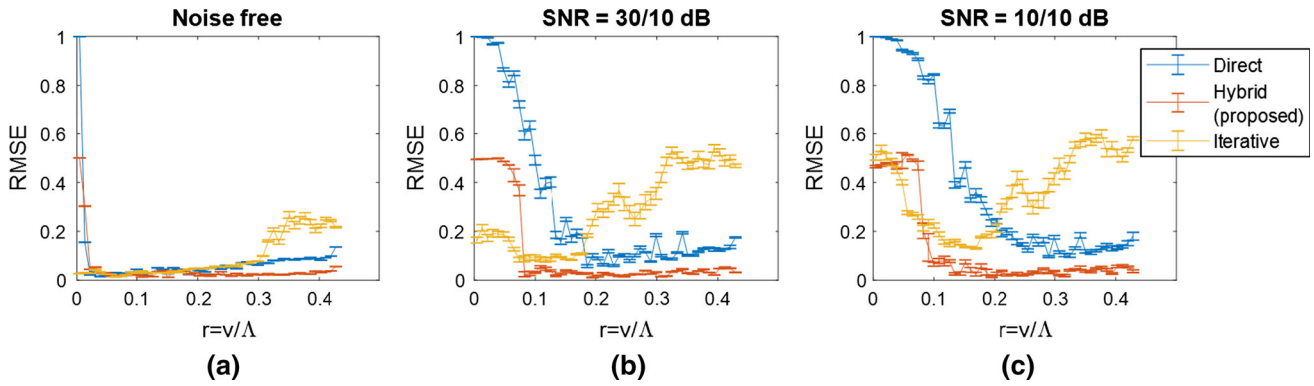

Fig. 5 RMSE of the reconstructions using the Direct, Iterative and proposed Hybrid method, in case of a homogeneous phantom for the following cases: **a** noise free, **b** SNR = 30 dB axial/10 dB lateral direction, and **c** SNR = 10 dB

certain ratios r, after which it increases again. For our proposed method, the RMSE does not appear to increase after this point. The Iterative method outperforms the Hybrid method up to $r < 0.1$, however, after $r > 0.1$ our Hybrid method outperforms both alternatives by up to 50% RMSE. Considering only the ranges where all methods were stable, our proposed method improves the RMSE by 11% compared to the other methods, for the simulated noisy acquisition. We repeated the previous study for the 4 kPa phantom with a single 8 kPa, 10 mm radius inclusion, as in Fig. 1b. Similar results were obtained (Fig. 6), where the proposed method improves the CNR by up to 11 dB in the noisy cases, for all $r > 0.1$. There was no significant difference between the Iterative and Direct methods in terms of reconstruction metrics, but it is important to note the smaller stable area of the former methods.

We tested whether the errors metrics between the methods are affected by the choice of the finite difference operator used, with no significant difference observed between the Gradient and Laplace finite difference operators, Fig. 7.

Simulations on a phantom with 3 inclusions (Fig. 1c) were intended to mimic varying stiffnesses that can be encountered in the same field of view. We investigated a noise-free and a noisy case with SNR=30 dB axial/10 dB lateral direction at r ratios of 0.05, 0.1 and 0.25. The RMSE of the reconstruction results and the profile through the center of the phantom are presented in Fig. 8. It can be seen that the proposed method achieves the best results over all three ranges. The profiles plotted in Fig. 8d show a sharper inclusion delineation compared to the other methods.

Ex vivo results

Ultrasound images were acquired using a SonixTouch Ultrasound machine (Ultrasonix Medical Corp., Richmond BC, Canada) and a SonixDAQ data receiver module. Harmonic mechanical excitation was used to excite tissue at a frequency of 75 Hz using a voice coil actuator (BEI KIMCO). A L14-5/38 128-element linear-array ultrasound transducer with a center-frequency of 5 MHz was used. Image acquisition was performed using a frame rate of 1 kHz, with SonixDAQ module, in plane wave configuration. We conducted our experiments on ex vivo bovine liver samples. Thermal ablation was emulated in this work by removing a small piece of liver tissue, thermally ablating it and then reinserting it at the removed location. The extracted piece had dimensions of 5 mm × 11 mm, and thermal ablation was induced by heating the extracted piece. The inclusion was barely visible in the B-mode image, as it is shown with a delineated circle in Fig. 9a. The inclusion is somewhat visible in all elastographic reconstructions, shown in Fig. 9b–d. In the Direct method, the inclusion is difficult to locate, with elasticity values considerably underestimated, hence making it almost invisible. The Iterative method leads to a better inclusion delineation; however, several other artifacts are seen in the image, in the center as well as near the boundaries. A piece-wise constant inclusion is clearly identified with the Hybrid method, with minimal boundary and background artifacts.

Discussion and conclusions

In the presented approach, we avoid direct inversion of the elasticity model (2), allowing a level of physical inconsistency of the elasticity parameters. Results from Fig. 4b allow us to conclude that it is feasible to demand a high level of physical plausibility (achieved with high values of ρ) only for low noise levels. By tuning this parameter, our method achieves higher noise robustness. The initial decrease in RMSE in Fig. 6, with increasing frequency, was shown in [16] to be due to a decrease of the effect of noise with increase in frequency. We hypothesis that the further decrease in quality metrics with frequency is because of the decreasing number of pixels per wavelength in the model displacement. The

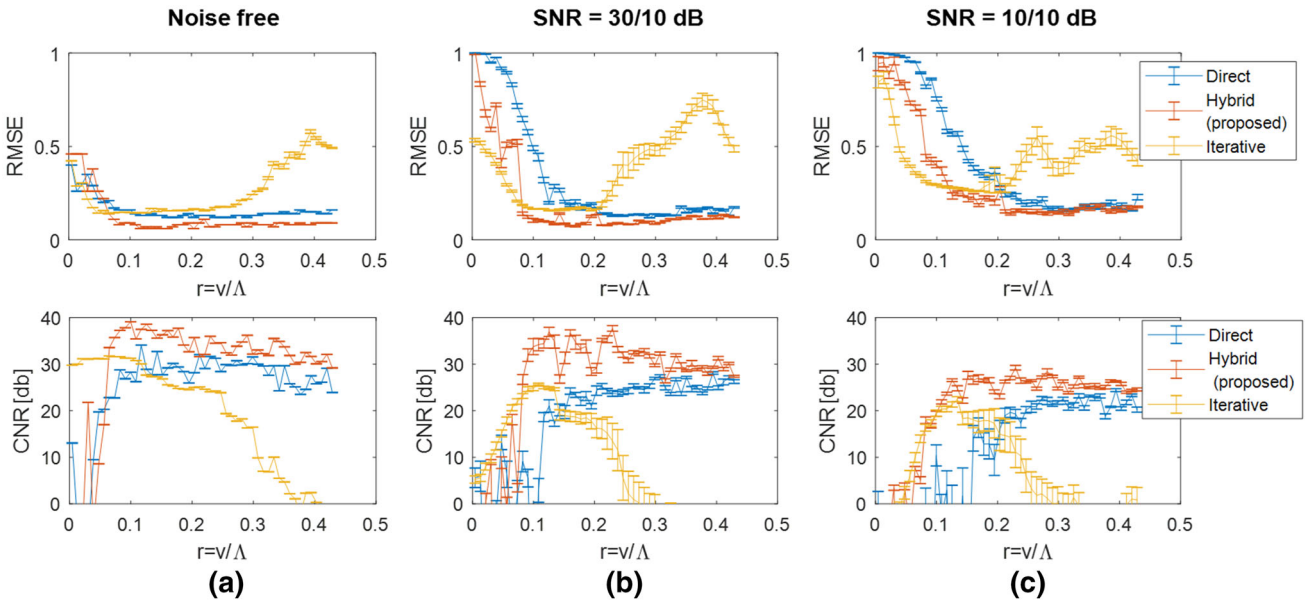

Fig. 6 RMSE and CNR of the reconstructions using the Direct, Iterative and the proposed Hybrid method in the case of a single 8 kPa inclusion inside a 4 kPa phantom for the following cases: **a** noise-free, **b** SNR = 30 dB axial/SNR = 10 dB lateral, and **c** SNR = 10 dB

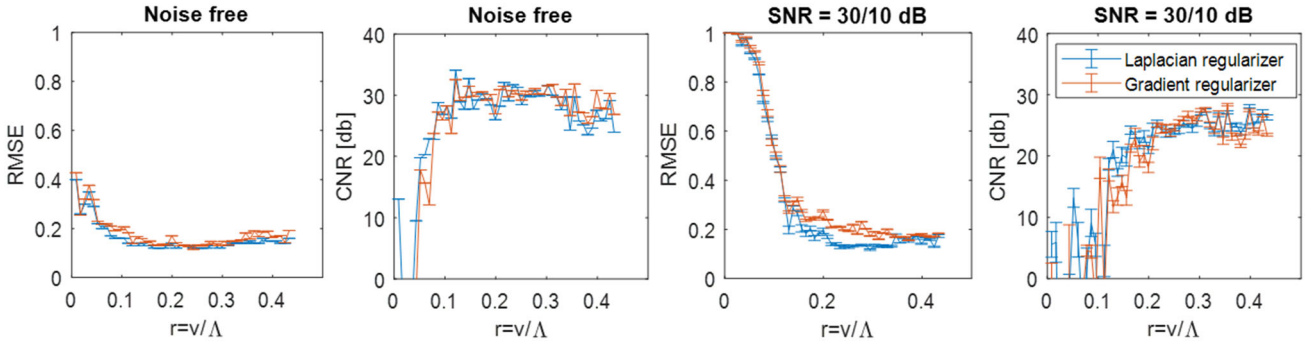

Fig. 7 RMSE and CNR of the reconstructions using a finite difference Laplacian (blue) and Gradient operator (red) regularizers in the case of a single 8 kPa inclusion inside a 4 kPa phantom for the following cases: noise-free, SNR = 30 dB axial/SNR = 10 dB lateral

stability of our method at various r ratios is observed in Fig. 8. We believe that it is more stable at lower frequencies compared to the direct method, as it does not require inertial forces, which are close to 0 at low frequencies, i.e. $\omega^2\mathbf{M} \rightarrow 0$. In the case of the Iterative method, it was shown in [16], that because (2),which contains a frequency term, has to be inverted, a larger number of nodes per wavelength are required for the method to converge, hence it is unstable at higher frequencies. The sharp inclusion delineation and elasticity underestimation of our method from Fig. 8 is to be expected due to the TV regularization.

In the case of ex vivo liver, the elasticity values using the Direct method were considerably underestimated, a similar effect can be seen in the phantom simulations in Fig. 8a, b. We assume that this was because the r ratio was below its stable region. Reconstruction artifacts can be observed in the Direct and Iterative method, possibly due to the L^2 regularization norm. In the Hybrid method, the inclusion is clearly delineated, however axis-aligned artifacts due to anisotropic TV regularization are present. To solve this, isotropic TV regularization could be implemented as future work. In the presented examples, TV yields better results due to its ability to emphasize contrast, important for ablation delineation.

Ablation can be a relatively slow process, with HIFU ablation of a single spot taking up to 12 s [25]. Our proposed method performs quasi real-time (a median reconstruction runtime of 3.7 s at a resolution of 2 × 2 mm for 40 × 40 mm field of view), that can be sufficient to facilitate elastographic imaging for ablation control. This is faster than the Iterative method ($<$ 15 s) and is comparable to the Direct method ($<$ 1 s), with the reconstructions performed with a Matlab implementation on an Intel Core i7, 4.00 GHz, 16 GB RAM machine.

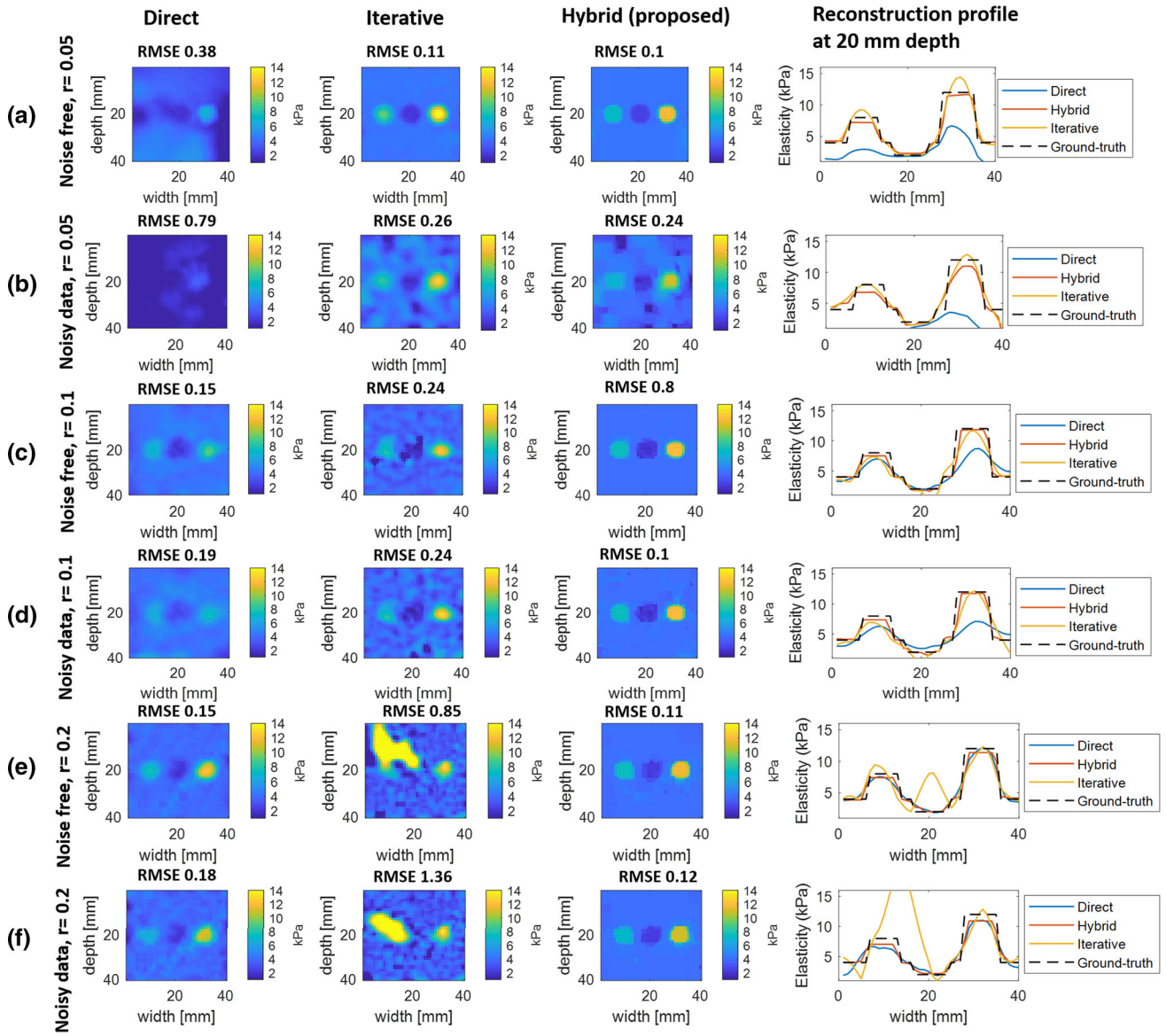

Fig. 8 Reconstruction results on a three 8 mm inclusion phantom, at three frequencies ($r = 0.05, 0.1, 0.25$ in noise-free and noisy conditions)

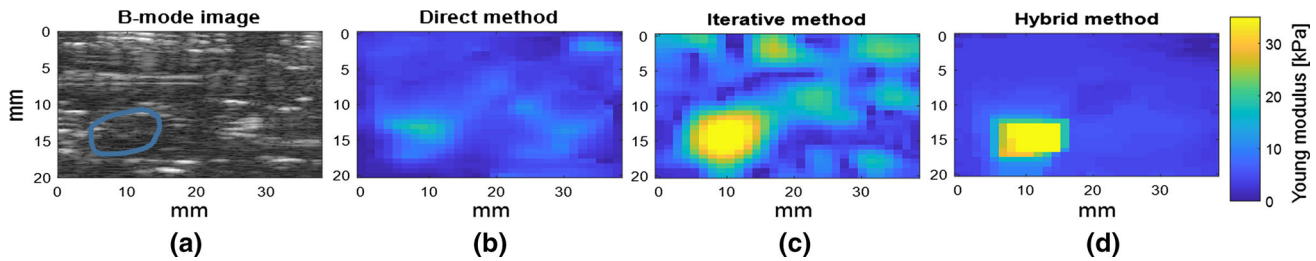

Fig. 9 **a** B-mode of the ex vivo liver, where the inclusion was manually delineated. Reconstruction results using the Direct (**b**), Iterative (**c**) and the proposed hybrid (**d**) method are presented

In this work, we presented a novel FEM inverse problem formulation which contains a data fidelity term, a physical constraint—the FEM discretized motion equation, and a TV spatial coherence regularization term, that was solved in an unconstrained optimization. Numerical phantom results indicate a stability for a wider range of frequencies or wavelengths and higher noise robustness, essential factors to consider in the case of medical procedures such as RF ablation. Reconstruction results were improved by up to 50% RMSE and 11 dB compared to other FEM-based methods. Our proposed method also improved lesion delineation in an ex vivo liver sample that was locally subjected to ablation.

Acknowledgements This work was funded by Swiss National Science Foundation (SNSF).

Compliance with ethical standards

Conflict of interest All authors declare no conflict of interest.

Research involving human participants No studies on human participants.

References

1. Arnal B, Pernot M, Tanter M (2011) Monitoring of thermal therapy based on shear modulus changes: II. Shear wave imaging of thermal lesions. IEEE Trans Ultrason Ferroelectr Freq Control 58(8):1603–1611
2. Babuška I, Suri M (1992) Locking effects in the finite element approximation of elasticity problems. Numer Math 62(1):439–463
3. Baki P, Sanabria SJ, Kosa G, Szekely G, Goksel O (2015) Thermal expansion imaging for monitoring lesion depth using m-mode ultrasound during cardiac rf ablation: in vitro study. Int J Comput Assist Radiol Surg 10(6):681–693
4. Castera L, Forns X, Alberti A (2008) Non-invasive evaluation of liver fibrosis using transient elastography. J Hepatol 48(5):835–847
5. Conn AR, Gould NI, Toint PL (2000) Trust region methods. SIAM, Philadelphia
6. Cooper J, Gimpelson RJ (2004) Summary of safety and effectiveness data from FDA: a valuable source of information on the performance of global endometrial ablation devices. J Reprod Med 49(4):267–273
7. Doyley M, Meaney P, Bamber J (2000) Evaluation of an iterative reconstruction method for quantitative elastography. Phys Med Biol 45(6):1521
8. Eskandari H, Salcudean SE, Rohling R (2008) Viscoelastic parameter estimation based on spectral analysis. IEEE Trans Ultrason Rerroelectr Freq Control 55(7):1611–1125
9. Ferraioli G, Parekh P, Levitov AB, Filice C (2014) Shear wave elastography for evaluation of liver fibrosis. J Ultrasound Med 33(2):197–203
10. Gazelle GS, Goldberg SN, Solbiati L, Livraghi T (2000) Tumor ablation with radio-frequency energy. Radiology 217(3):633–646
11. Goksel O, Eskandari H, Salcudean SE (2013) Mesh adaptation for improving elasticity reconstruction using the fem inverse problem. IEEE Trans Med Imaging 32(2):408–418
12. Goldberg SN, Dupuy DE (2001) Image-guided radiofrequency tumor ablation: challenges and opportunities part I. J Vasc Interv Radiol 12(9):1021–1032
13. Haissaguerre M, Jais P, Shah DC, Gencel L, Pradeau V, Garrigues S, Chouairi S, Hocini M, Métayer P, Roudaut R, Clementy J (1996) Right and left atrial radiofrequency catheter therapy of paroxysmal atrial fibrillation. J Cardiovasc Electrophysiol 7(12):1132–1144
14. He DS, Zimmer JE, Hynynen K, Marcus FI, Caruso AC, Lampe LF, Aguirre ML (1994) Preliminary results using ultrasound energy for ablation of the ventricular myocardium in dogs. Am J Cardiol 73(13):1029–1031
15. Honarvar M, Lobo J, Mohareri O, Salcudean S, Rohling R (2015) Direct vibro-elastography fem inversion in cartesian and cylindrical coordinate systems without the local homogeneity assumption. Phys Med Biol 60(9):3847
16. Honarvar M, Rohling R, Salcudean S (2016) A comparison of direct and iterative finite element inversion techniques in dynamic elastography. Phys Med Biol 61(8):3026
17. Honarvar M, Sahebjavaher R, Salcudean S, Rohling R (2012) Sparsity regularization in dynamic elastography. Phys Med Biol 57(19):5909
18. Hoskins PR, Martin K, Thrush A (2010) Diagnostic ultrasound: physics and equipment. Cambridge University Press, Cambridge
19. Konishi K, Nakamoto M, Kakeji Y, Tanoue K, Kawanaka H, Yamaguchi S, Ieiri S, Sato Y, Maehara Y, Tamura S (2007) A real-time navigation system for laparoscopic surgery based on three-dimensional ultrasound using magneto-optic hybrid tracking configuration. Int J Comput Assist Radiol Surg 2(1):1–10
20. Lencioni R, Cioni D, Bartolozzi C (2001) Percutaneous radiofrequency thermal ablation of liver malignancies: techniques, indications, imaging findings, and clinical results. Abdom Imaging 26(4):345–360
21. Liu DC, Nocedal J (1989) On the limited memory BFGS method for large scale optimization. Math Program 45(1):503–528
22. Livraghi T, Solbiati L, Meloni MF, Gazelle GS, Halpern EF, Goldberg SN (2003) Treatment of focal liver tumors with percutaneous radio-frequency ablation: complications encountered in a multicenter study. Radiology 226(2):441–451
23. Mariani A, Kwiecinski W, Pernot M, Balvay D, Tanter M, Clement O, Cuenod C, Zinzindohoue F (2014) Real time shear waves elastography monitoring of thermal ablation: in vivo evaluation in pig livers. J Surg Res 188(1):37–43
24. McRury ID, Haines DE (1996) Ablation for the treatment of arrhythmias. Proc IEEE 84(3):404–416
25. Orsi F, Arnone P, Chen W, Zhang L (2010) High intensity focused ultrasound ablation: a new therapeutic option for solid tumors. J Cancer Res Ther 6(4):414
26. Parikh N, Boyd S (2014) Proximal algorithms. Found Trends Optim 1(3):127–239
27. Park E, Maniatty AM (2006) Shear modulus reconstruction in dynamic elastography: time harmonic case. Phys Med Biol 51(15):3697
28. Pethig R, Kell DB (1987) The passive electrical properties of biological systems: their significance in physiology, biophysics and biotechnology. Phys Med Biol 32(8):933
29. Rivaz H, Fleming I, Assumpcao L, Fichtinger G, Hamper U, Choti M, Hager G, Boctor E (2008) Ablation monitoring with elastography: 2D in-vivo and 3D ex-vivo studies. Med Image Comput Comput Assist Interv MICCAI 2008:458–466
30. Sandrin L, Fourquet B, Hasquenoph JM, Yon S, Fournier C, Mal F, Christidis C, Ziol M, Poulet B, Kazemi F (2003) Transient elastography: a new noninvasive method for assessment of hepatic fibrosis. Ultrasound Med Biol 29(12):1705–1713
31. Sarvazyan AP, Rudenko OV, Swanson SD, Fowlkes JB, Emelianov SY (1998) Shear wave elasticity imaging: a new ultrasonic technology of medical diagnostics. Ultrasound Med Biol 24(9):1419–1435

32. Souchon R, Bouchoux G, Maciejko E, Lafon C, Cathignol D, Bertrand M, Chapelon JY (2005) Monitoring the formation of thermal lesions with heat-induced echo-strain imaging: a feasibility study. Ultrasound Med Biol 31(2):251–259
33. Tzschätzsch H, Trong MN, Scheuermann T, Ipek-Ugay S, Fischer T, Schultz M, Braun J, Sack I (2016) Two-dimensional time-harmonic elastography of the human liver and spleen. Ultrasound Med Biol 42(11):2562–2571
34. Wang Z, Aarya I, Gueorguieva M, Liu D, Luo H, Manfredi L, Wang L, McLean D, Coleman S, Brown S (2012) Image-based 3D modeling and validation of radiofrequency interstitial tumor ablation using a tissue-mimicking breast phantom. Int J Comput Assist Radiol Surg 7(6):941–948
35. Webster JG, Hendee WR (1989) Encyclopedia of medical devices and instrumentation, volumes 1 4. Phys Today 42:76
36. Whayne JG, Nath S, Haines DE (1994) Microwave catheter ablation of myocardium in vitro. Assessment of the characteristics of tissue heating and injury. Circulation 89(5):2390–2395
37. Zienkiewicz OC, Taylor RL (2000) The finite element method: solid mechanics, vol 2. Butterworth-Heinemann, London